

# Thrust-fault growth and segment linkage in the active Ostler fault zone, New Zealand

Kenneth Davis<sup>a</sup>, Douglas W. Burbank<sup>a,\*</sup>, Donald Fisher<sup>b</sup>, Shamus Wallace<sup>c,1</sup>, David Nobes<sup>c</sup>

<sup>a</sup>Department of Geological Sciences, University of California at Santa Barbara, Santa Barbara, CA 93106, USA

<sup>b</sup>Department of Geosciences, Pennsylvania State University, University Park, PA 16802, USA

<sup>c</sup>Department of Geological Sciences, University of Canterbury, Private Bag 4800, Christchurch, New Zealand

Received 23 September 2003; received in revised form 19 April 2005; accepted 19 April 2005

Available online 6 July 2005

## Abstract

Thrust faulting is a fundamental mode of crustal deformation, yet many of the key geometrical attributes of thrust faults and the controls on fault rupture, growth, and linkage remain poorly resolved. Numerous surface-rupturing thrust faults cut through upper Quaternary glacial outwash terraces within the Ostler Fault zone, an active thrust system in the Southern Alps, New Zealand. We use these deformed marker surfaces to define the three-dimensional deformation field associated with their surface expression and to map displacement and length on ~40 fault segments. Displacement transfer across two fault segment arrays occurs in distinctly different styles. In one, displacement is transferred between en échelon fault segments to produce a smooth, linear displacement gradient. In the other, large-scale folding and a population of small faults transfer displacement between two non-overlapping fault segments, with a residual displacement minimum within the transfer zone. Size distribution of fault-segment length and maximum displacement follow a power-law scaling relationship. Maximum displacement ( $D_{\max}$ ) scales linearly with and represents ~1% of segment trace length ( $L$ ).  $D_{\max}/L$  data from the segments of the Ostler Fault zone display similar scaling to a global fault dataset. This similarity is surprising, given that the observed displacements along the Ostler Fault represent only 20 ky of slip on fault segments that are likely to be many times older.

© 2005 Published by Elsevier Ltd.

**Keywords:** Distributed strain; Fault populations; Fault scaling; Displacement–length scaling; Ostler Fault; MacKenzie Basin

## 1. Introduction

The development of fault zones is a fundamental process in tectonics, with implications ranging from interpretation of seismic data to estimating brittle strain (Scholz, 1990). Nevertheless, the ways in which faults rupture, grow, and link remain poorly resolved. Extensive datasets from normal fault systems (Dawers and Anders, 1995; Manighetti et al., 2001; Walsh et al., 2003) have been used to examine fault populations with a large range in scale and relatively uniform tectonic and lithologic boundary conditions, thereby providing reliable tests of fault-growth models and fault-scaling laws for normal faults. Some of the more

detailed studies consider systems of faults that are very well exposed, but are only a few meters in length (Soliva and Benedicto, 2004). At the scale of small outcrops, fully three-dimensional exposures can permit reliable documentation of distributed displacement within isolated, linked, and breached faults and ramps. Few temporal data are commonly available with such studies, and the reliability of extrapolating from metric scales to the larger spatial arrays of faults is usually unknown.

Few studies, moreover, investigate the detailed character of thrust-fault populations or their along-strike fault-displacement patterns. Most studies utilize cross-sections through ancient thrust faults, and their ability to resolve along-strike variations in displacement is limited as hanging wall cutoffs are commonly eroded and only exposed near the fault terminations (e.g. Elliott, 1976). Due to scarce data, key questions about thrust-fault growth and scaling remain unresolved. (1) How does displacement vary along the strike of a thrust fault? (2) How is displacement distributed and transferred among multiple segments (Fig. 1) within a fault

\* Corresponding author. Tel.: +1 805 893 7858; fax: +1 805 893 8649.

E-mail address: burbank@crustal.ucsb.edu (D.W. Burbank).

<sup>1</sup> Present address: Tonkin and Taylor, PO Box 1009, Nelson, New Zealand.

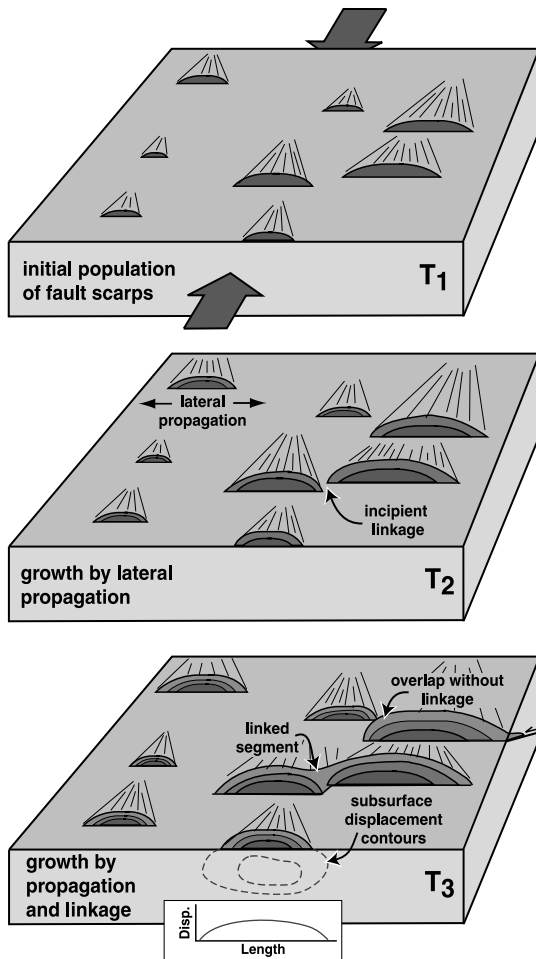


Fig. 1. Schematic illustration of fault scarp development through repeated earthquakes. At T1, fault scarps form on a block under compressive stress. These scarps become higher and longer as displacement accumulates and fault tips propagate (T2). Eventually, some faults coalesce and link, joining two scarps (T3). A displacement gradient occurs on the fault planes, with a maximum displacement somewhere below the surface. Displacement and length measured at the surface (as in this study) offer only a proxy of true maximum displacement (inset plot).

zone? (3) How much strain occurs in the hanging walls of thrust faults, and how does this strain vary along strike? (4) What are the scaling laws for lengths and displacements of thrust fault segments? (5) What is the length–displacement relationship and displacement profile for active fault segments over thousands of years, and how do these datasets compare with the length–displacement relationship of a kinematically linked fault system in the long term?

In this paper, we characterize the geometry and scaling of fault segment length and displacement in an active, segmented thrust fault zone in New Zealand (Fig. 2), and we evaluate these results in the context of fault-growth and fault-segmentation models. Excellent exposure of the surface fault trace, as it disrupts a regionally extensive geomorphic marker surface, allows detailed along-strike displacement profiles to be constructed (Fig. 2c). We focus on two zones of thrust-fault linkage to illustrate how

displacement is transferred across the zones and determine the effects of segment interaction on the fault-displacement profiles. Finally, we calculate scaling relationships for both the fault segment-size distribution and  $D_{\max}$  versus  $L$  for fault segments.

## 2. Fault scaling

Displacement profiles along faults can provide insight into fault-growth history and the effects of fault interaction (Peacock and Sanderson, 1991; Dawers and Anders, 1995; Gupta and Scholz, 1998, 2000; Manighetti et al., 2001). For some fault systems, characteristics such as fault-zone width, length, and displacement appear to obey simple scaling relationships as illustrated by global datasets of fault length ( $L$ ) and maximum fault displacement ( $D_{\max}$ ), primarily from normal faults (Scholz, 1990; Gillespie et al., 1992; Schlische et al., 1996).

Based on studies of natural fault populations, the distribution of both  $L$  and  $D_{\max}$  are argued to follow a power-law relationship:

$$N(S) = KS^{-C}, \quad (1)$$

where  $N(S)$  is the cumulative number of faults with a characteristic size (measured by  $L$  or  $D_{\max}$ ) larger than  $S$ , and  $K$  and  $C$  are constants (Scholz and Cowie, 1990; Scholz et al., 1993; Cladouhos and Marrett, 1996; Nicol et al., 1996a; Poulimenos, 2000). Increasing values of  $C$  denote a greater number of small faults relative to large faults. Empirical values for  $C$  of individual datasets range from 0.67 to 2.07 (Cladouhos and Marrett, 1996; Nicol et al., 1996a), but the validity of calculating a universal  $C$ -value by combining datasets from different fault types and settings has been questioned (Watterson et al., 1996). In particular, combining one- and two-dimensional datasets may be misleading. Furthermore,  $C$ -values may decrease with time as a fault zone matures and becomes more dominated by large faults (Cowie et al., 1995; Cladouhos and Marrett, 1996; Nicol et al., 1996a). Power-law, cumulative fault size–frequency distributions underscore the fractal nature of fault systems and suggest that fault characteristics are a direct consequence of seismic rupture properties, i.e. the power-law Gutenberg–Richter earthquake frequency–magnitude distribution (Turcotte, 1992; Oncel et al., 2001).

The relationship between  $L$  and  $D_{\max}$  is also commonly written as a power-law:

$$D_{\max} = kL^n, \quad (2)$$

where  $k$  and  $n$  are constants. The considerable scatter and limited scale range of existing fault datasets, along with doubts about the validity of comparing datasets from different tectonic and lithological settings, have hindered efforts to discern whether or not a universal value of  $n$  exists. Estimates for the value of  $n$  have ranged as high as 2 (Walsh and Watterson, 1988; Nicol et al., 1996a), but several

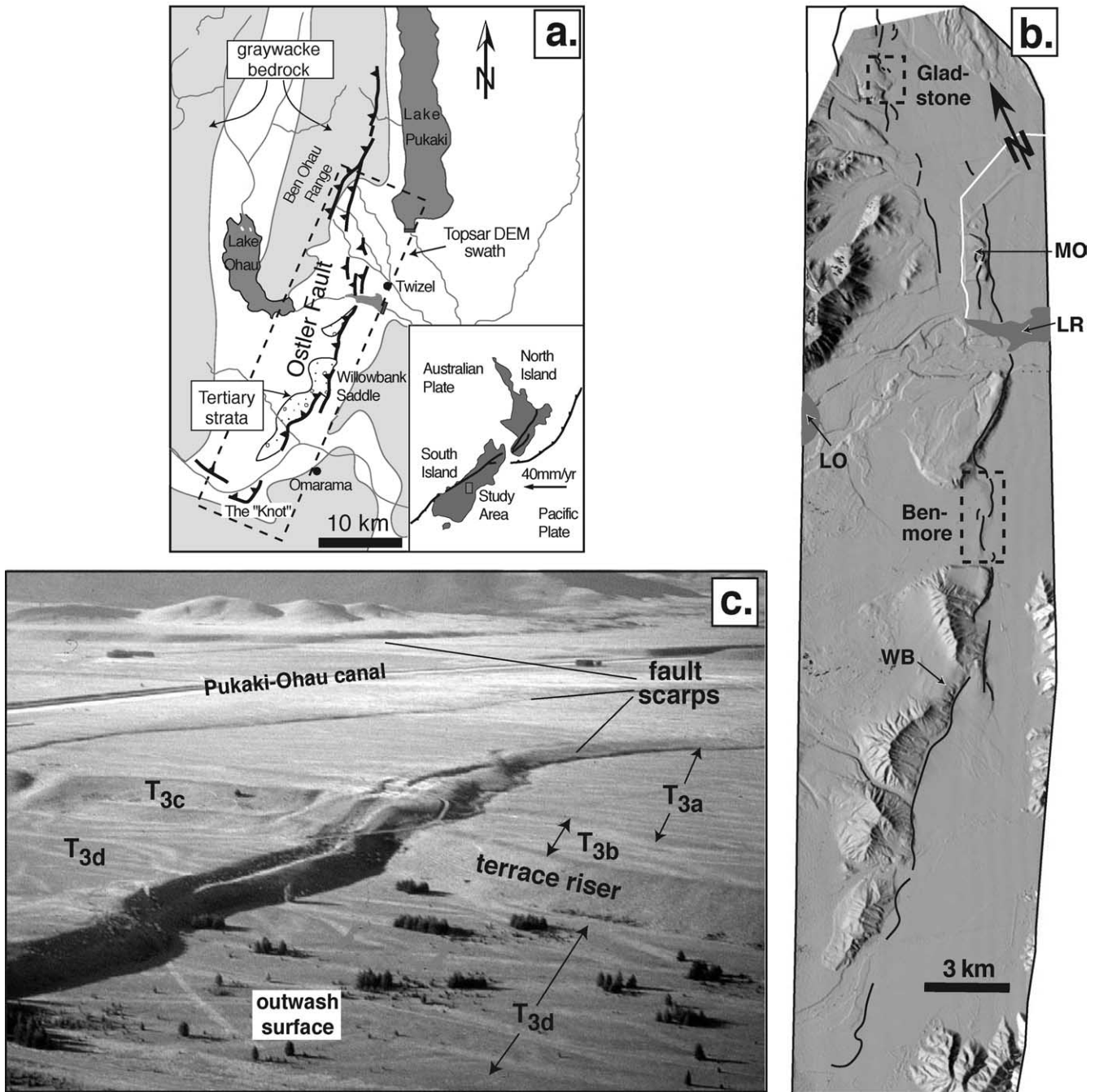


Fig. 2. The Ostler Fault zone (OFZ). (a) Map showing the primary surface trace of the OFZ and approximate extent of Torlesse meta-sedimentary basement and Tertiary uplifts in the MacKenzie Basin. Unshaded area is primarily Quaternary till and glacial outwash deposits. Inset shows location of the OFZ on the eastern side of the Southern Alps. (b) Shaded relief image from 10-m TOPSAR DEM of the east-vergent OFZ. Locations of the Benmore and Gladstone arrays, which were studied in detail, are boxed. LR: Lake Ruataniwha; LO: Lake Ohau; MO: Mt Ostler; WB: Willowbank Saddle. (c) Oblique aerial photograph of three fault scarps between Lake Ruataniwha and Mt Ostler displacing glacial outwash surfaces. Note the succession of terraces on the outwash surface ( $T_{3a}$ – $T_{3d}$ ) formed by downcutting of the Ohau River. The largest of the scarps, in the foreground, has a vertical offset of  $\sim 15$  m.

theoretical and empirical studies suggest that the scaling is approximately linear ( $n=1$ ) (Cowie and Scholz, 1992b; Dawers et al., 1993; Scholz et al., 1993; Clark and Cox, 1996; Schlische et al., 1996; Manighetti et al., 2001). Although controversy exists concerning whether scaling for larger faults ( $> 100$  m) is non-linear (Nicol et al., 1996a), this relationship has led to fault growth models (Fig. 1)

where faults begin as isolated cracks and grow self-similarly until they interact with neighbors in zones of overlap at which point lateral growth is retarded until linkage removes the slip deficit (Gupta and Scholz, 2000). An alternative growth model involves early establishment of fault lengths with subsequent increases in maximum displacements that shift the fault population in the long term away from the

trend defined by the slip distribution of earthquakes (Walsh et al., 2002).

Theoretical models of dislocations in elastic–plastic solids predict a quasi-elliptical (Pollard and Segall, 1987) or bell-shaped (Cowie and Scholz, 1992a) along-strike displacement profile with zero displacement at the crack tips and maximum displacement near the center of the crack. Although theoretical models successfully predict some basic displacement profile characteristics, data from real faults show significant variability in profile shape and location of maximum displacement (Dawers and Anders, 1995; Manighetti et al., 2001). Mechanical interaction and linkage among fault segments have a first-order effect on the accumulation of fault displacement and may account for a large portion of this observed variability in displacement profile shape (Cartwright et al., 1995; Gupta and Scholz, 2000). Spatial arrays of fault-displacement profiles can serve to delineate the mechanism of fault-segment interaction and linkage in natural fault systems (Fig. 1), where mechanical interaction of segments can produce smooth gradients of total displacement along a fault zone (Childs et al., 1995; Dawers and Anders, 1995; Crider and Pollard, 1998; Manighetti et al., 2001; Soliva and Benedicto, 2004).

Because most previous fault-scaling studies have focused on normal fault populations, the behavior of thrust fault systems remains poorly explored. In this study, we exploit a particularly well-exposed thrust-fault system to develop statistics on fault length, displacement, and displacement transfer.

### 3. Study area

The Ostler fault zone (OFZ) is located in the intermontane Mackenzie Basin on the east flank of the Southern Alps, New Zealand (Fig. 2). Of the  $\sim 40$  mm/yr of oblique convergence between the Pacific and Australian plates, most deformation is accommodated by the Alpine Fault, west of the Southern Alps (Walcott, 1998; Tippett and Hovius, 2000; Norris and Cooper, 2001). Approximately one-third of the predicted relative plate motion occurring on the South Island is partitioned into structures east of the Southern Alps (Tippett and Hovius, 2000), such as the OFZ.

Bedrock in the vicinity of the Mackenzie Basin is predominately Torlesse greywacke, which crops out at the surface in the Ben Ohau Range west of the OFZ. In the basin, up to 1 km of Cenozoic sediment lies above bedrock (Read, 1984; Long et al., 2000). These sediments include semi-indurated Neogene sand and gravel and poorly indurated Pleistocene glacial outwash. Depth and character of sediments in the basin are highly variable and represent a poorly known control on the fault mechanics of the OFZ.

The geomorphic surface of the Mackenzie Basin is dominated by glacial outwash plains and fluvial terraces from at least three Pleistocene glaciations (Read, 1984; Blick et al., 1989). All the fluvial terraces utilized in this study originated as straths beveled across either Tertiary

strata or older Quaternary fill. Coarse gravels, ranging in thickness from a few meters to several tens of meters, subsequently covered the straths. These regionally extensive surfaces are blanketed in shortgrass, mostly undissected, and intricately textured with outwash channels (Fig. 2c). In short, they provide a pristine marker of deformation on the OFZ. Since these surfaces were created during the last glaciation, downcutting has occurred on major streams such as the Ohau River and produced flights of terraces that have been subsequently deformed by the OFZ (Fig. 2c). In addition to the last-glacial surfaces, older uplifts are present on the hanging wall of the OFZ. These uplifts are more dissected than the last-glacial outwash surfaces, but in some cases, original planar terrace surfaces are preserved on them. Loess is present in variable amounts on both the last-glacial surfaces and older uplifts, and is typically 0–0.5 m thick.

The dataset used in this study was collected from a series of NNE-trending fault scarps that displace these outwash surfaces. Scarps range in height from less than a meter to  $\sim 100$  m, although the largest scarps are not well exposed where they cut older glacial surfaces and are not included in the dataset. The scarps are mostly west-side-up and are interpreted to have formed by surface rupture and fault-related folding on east-vergent thrust faults (Fig. 2). Because few cross-sections of faults are exposed in the field area, fault dip measurements were collected where scarps could be aligned across multiple river terraces. These offsets define an average fault dip near the surface of  $50 \pm 9^\circ$  ( $n=4$ ), which is consistent with dips measured from migrated ground-penetrating radar profiles (Nobes et al., 2003). Numerous outwash channels that cross the fault trace exhibit no lateral offset and indicate that strike-slip motion is negligible. Fault segments of the OFZ display varying states of interaction with linked, overlapping, or spatially isolated fault traces (Soliva and Benedicto, 2004).

Off-fault deformation is also observed in the OFZ. Warped geomorphic surfaces reveal fault-related folding in the hanging wall of some fault segments, especially those farther from the mountain front where basin sediments are presumably thicker. Typical folds are gentle (interlimb angle  $\sim 170$ – $175^\circ$ ), upright to slightly east-vergent, and have wavelengths of  $\sim 100$ – $500$  m. On a larger scale, geomorphic surfaces in the hanging wall are backtilted over  $\sim 1$ – $5$  km west of the fault trace, suggesting rotation on a listric fault that steepens to the east.

All the preserved geomorphic surfaces are younger than the initiation of faulting on the OFZ. Therefore, on a given geomorphic surface, a fault scarp only records the displacement that accumulated after formation of the surface. The measured fault trace length, however, likely represents the total length since the segment originated. Evidence for Holocene deformation on the Ostler Fault is abundant, and trenching studies indicate that paleoseismic events occurred  $\sim 3000$  and  $\sim 6000$  years before present (Van Dissen et al., 1993). Although little evidence exists to

determine whether the entire OFZ ruptured in each of the past earthquakes, we consider the entire system to be kinematically linked. Many of the individual fault traces at the surface probably merge downward into a single slip surface. Consequently, what may appear to be an isolated fault trace at the surface might more properly be considered a fault segment.

Based on estimates of surface ages from Read (1984), we calculate average displacement rates for two areas based on the maximum fault displacement observed at the surface. The  $> 120$  ka Willowbank Saddle surface (Fig. 2) is offset  $\sim 100$  m from the basin floor, yielding a maximum vertical displacement rate of 0.8 mm/yr, whereas the  $> 22$  ka Benmore surface is offset 15 m, with a maximum vertical displacement rate of 0.7 mm/yr. These rates are slightly lower, but similar to geodetic observations of a  $\sim 1$  mm/yr rock-uplift rate of the hanging wall from fold growth or fault creep on some segments of the fault (Blick et al., 1989).

Of the ca. 38 mm/yr relative plate motion in the South Island (DeMets et al., 1994), only  $\sim 27$  mm/yr is accommodated on or near the Alpine Fault, with the remaining  $\sim 11$  mm/yr distributed in the Pacific Plate along a wide zone east of the Alpine Fault (Norris and Cooper, 2001). Therefore, if geologic shortening rates across the OFZ calculated from terrace surface offsets are about 0.7–1 mm/yr (assuming fault dip of  $\sim 50^\circ$ ), the OFZ may accommodate up to  $\sim 5$ –10% of the intra-Pacific Plate deformation.

#### 4. Methods

Forty fault scarps were surveyed using a Trimble 4700 differential GPS with centimeter-scale vertical and horizontal precision. Simultaneous tandem surveys along the top and base of each scarp provided horizontal and vertical coordinates every 1–3 m that were, in turn, used to generate

detailed scarp height versus length plots (Figs. 3 and 4). Scarp height is used as a proxy for fault displacement (as opposed to vertical throw) following two corrections. First, the slope of the offset geomorphic surface is used to calculate the separation between the hanging wall and footwall surfaces (Fig. 3). Second, an estimate of fault dip ( $50 \pm 9^\circ$ ) is used to calculate fault slip at each point along the scarp. The largest displacement for each fault segment,  $D_{\max}$ , and the total trace length,  $L$ , are used in the fault segment-scaling statistics. Error in the  $D_{\max}$  calculation was estimated using a Monte Carlo simulation method. Uncertainties in the measurement of vertical offset and horizontal position with respect to the scarp, geomorphic surface slope, and fault dip (Fig. 3) are used to generate a probability distribution of  $D_{\max}$  values and its standard deviation.

Only fault scarps cutting Last Glacial age geomorphic surfaces are measured. Therefore, the scarps have a maximum age  $\sim 20$  ka (Read, 1984). In addition, only scarps where the displacement decreased to near zero at the tips are used (i.e. ‘tip–tip’ faults) (Fig. 4a). Notable exceptions are scarps where one tip is obscured by erosion near the end of the scarp ( $n=9$ ). Their maximum trace length is extrapolated from the displacement profile such that these ‘one-tip’ faults have error bars associated with both  $L$  and  $D_{\max}$  (Fig. 4b). All the fault scarps surveyed represent displacements along fault segments that are embedded within the larger OFZ.

Along-strike variation in magnitude of fault-related folding is analyzed by two methods: fold height and fold area. An implicit assumption in both methods is that the geomorphic surface on which topographic profiles of folds were measured mimics the strain from folding. This assumption is reasonable because folded, but continuous, outwash channels and terrace risers are commonly observed on the hanging wall of the OFZ. Fold height is calculated by subtracting the elevation difference between the hanging

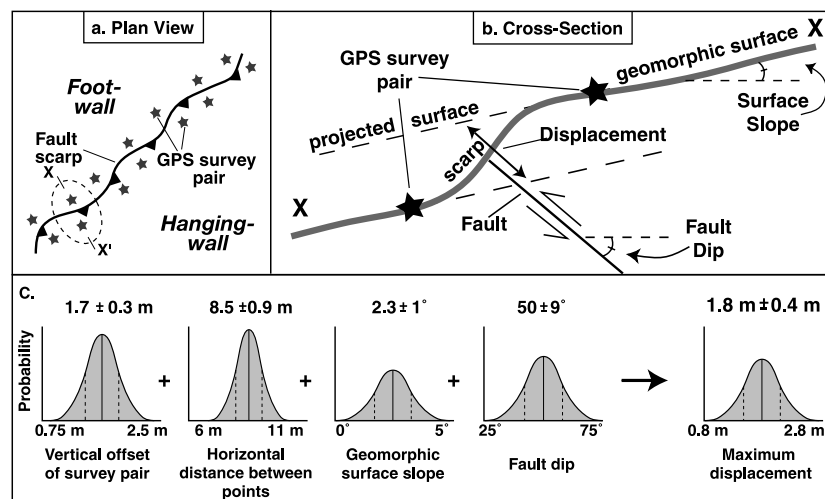


Fig. 3. Method for estimating fault displacement along a fault scarp. (a) GPS survey points are taken on the hanging wall and footwall, every 1–3 m. (b) Using estimates of geomorphic surface slope from fault-normal topographic profiles, an estimate for fault dip ( $50 \pm 9^\circ$ ) from field measurements, and positional data from GPS survey points, displacement is calculated at each GPS survey pair. (c) Monte Carlo simulation method for modeling  $D_{\max}$  error for one fault (BM 21). Each measurement is assigned a probability distribution, and 10,000 simulations are performed to calculate  $D_{\max}$  probability distribution.

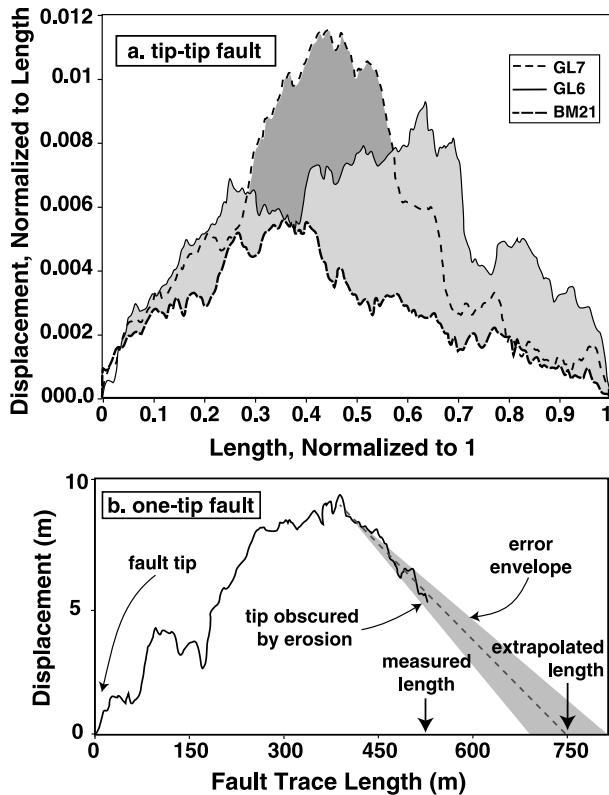


Fig. 4. (a) Example normalized displacement–length profiles ( $D$ – $L$ ) of OFZ fault segments illustrating quasi-elliptical (GL 6) and triangular (BM 21, GL 7) shapes and linear displacement gradients. (b) Method for extrapolating length of scarps where  $D$ – $L$  profile is incomplete (one-tip faults).

wall fold crest and the footwall on a TOPSAR DEM with a 10-m grid, with a correction that accounts for the  $\sim 1^\circ$  slope of the undeformed geomorphic surface. Total fault offset is then subtracted, and the resulting fold height is a measure of amplitude of the fold crest above a restored, unfaulted geomorphic surface. The second method geometrically estimates the magnitude of a fault-displacement gradient (Suppe and Medwedeff, 1990; Wickham, 1995) that would produce a given fold by conserving fold cross-sectional area. Fold area and length are estimated graphically from topographic profiles and incremental contributions from faults cutting the surface are subtracted in order to calculate the fault slip on a  $50^\circ$ -dipping fault that is required to conserve area (Fig. 5). This method has the advantage of estimating a displacement that can be directly compared or summed with displacement measured from fault scarps. Monte Carlo error estimates for folding combine uncertainty in fold cross-sectional area, surface faulting, fold length and fault dip.

## 5. Results

### 5.1. Displacement profiles and transfer zones

Along-strike displacement profiles were surveyed on  $\sim 40$  fault segments within the OFZ. Individual profiles all

increase to a maximum displacement ( $D_{\max}$ ) somewhere within the fault trace and decrease to measurable displacements of near zero at the tips (Fig. 4a), except for one-tip faults where length is extrapolated from the displacement profile (Fig. 4b). Beyond these general characteristics, displacement profiles show a wide variety of shapes from quasi-elliptical to triangular to box-shaped. Many profiles show significant asymmetry. Low-amplitude variations in calculated displacement are present on all profiles and are probably due to topographic irregularities along the surveyed surfaces and to localized erosion of the fault scarp by recent or abandoned stream channels. Some profiles show larger scale irregularities and multiple displacement maxima, which may be the result of segment linkage and interaction (Peacock and Sanderson, 1991; Scholz et al., 1993; Cartwright et al., 1995; Dawers and Anders, 1995; Willemse et al., 1996).

Many fault segments in the OFZ constitute segment arrays, or spatially associated groupings of surface faults. When displacement profiles of individual segments are plotted and summed in a common projection, two arrays, the Gladstone array and Benmore array, reveal very different mechanisms for displacement transfer between fault segments.

The Gladstone array (Fig. 2) consists of four en échelon fault segments, with lengths of 230–800 m and maximum displacements of 2–7 m (Fig. 6). The total length of the array is  $\sim 1600$  m. The segments overlap 60–170 m and are separated by 10–80 m in the overlap zone. In two of the three overlap zones, segment tips curl around toward each other, reminiscent of elastic crack behavior observed on scales from millimeters in rock fracture experiments to kilometers on mid-ocean ridge segments and inferred to result from out-of-plane crack interactions (Sempere and Macdonald, 1986). We hypothesize that these fault segments are likely to merge downdip into a single slip surface.

The fault segments in the Gladstone array are organized such that the summed displacement forms a smoothly changing, linear, asymmetric profile (Fig. 6). Beginning with the maximum displacement of  $\sim 7$  m at the far southern end of the array, a linear displacement gradient extends northward from the  $D_{\max}$  to the array tip. Where displacement on an individual segment diminishes toward its tips, displacements on the overlapping segments increase, such that, for the most part, displacement minima do not occur in the overlap zones, and displacement varies smoothly between segments. Several segments (1, 2, and 4) display an apparently steepened displacement gradient in zones of tip interaction ('displacement anomalies' as predicted by Gupta and Scholz (2000)). The summed array has a  $D_{\max}/L$  ratio of 0.005; about half of the  $D_{\max}/L$  ratio for individual segments of the array.

In the Benmore array (Fig. 2), displacement is also transferred between fault segments, but the system is organized differently from the Gladstone array. Here, a  $\sim 20$ -ka outwash surface is deformed by two main thrust segments that converge, but do not overlap, in a slip-transfer

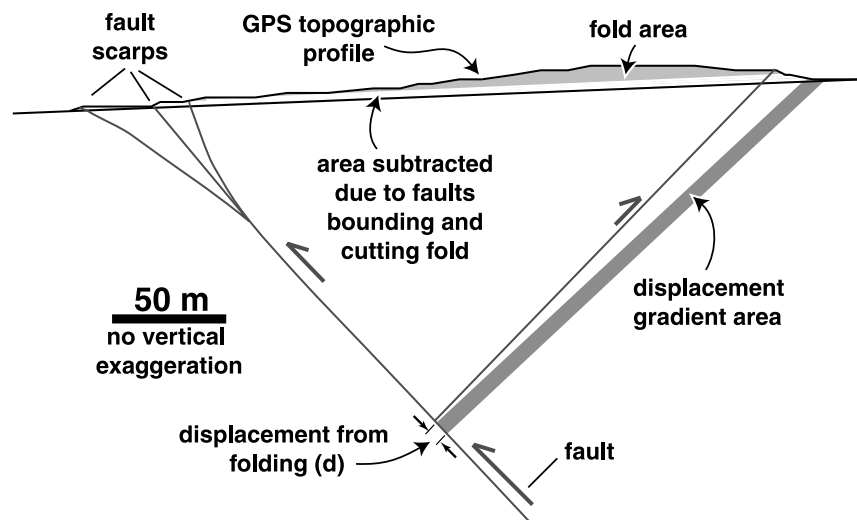


Fig. 5. Method for estimating displacement from folding. Fold cross-sectional area is calculated and area attributed to slip on faults cutting the surface is subtracted. The remaining cross-sectional area is equated with the area produced by a displacement gradient on the fault. By assuming a fault dip, displacement from faulting,  $d$ , is then calculated.

zone (Fig. 7a). Approximately 12 subparallel, small reverse faults with the same vergence as the main segments, termed ‘damage zone’ faults (Nicol et al., 1996a), cut the transfer zone. Hanging wall folding persists along the entire length of the two main segments. A 400-m-long backthrust bounds the transfer zone on the west (Fig. 7a). The main fault segments have lengths of 1600 and > 500 m and maximum displacements of 14 and 7 m. Toward the south, the southern main segment intersects a higher terrace surface on the outwash plain, such that relative displacement can only be compared accurately for the northernmost 500 m. The damage-zone faults are 30–300 m long and show maximum displacements of 1–3 m. Although the displacement on the backthrust and damage-zone faults is concentrated in the transfer zone of the two main segments, a displacement minimum also occurs in this transfer zone (Fig. 7b).

### 5.2. Fault-related folding

A hanging wall anticline warps the outwash surface along much of the Benmore array (Fig. 7a). One-fold axis extends from the tip of the southern main segment and plunges to the north. Another axis is present west of the main northern segments and plunges to the south. Fold height, defined as the elevation difference between the fold crest and the footwall minus the summed height of the fault scarp(s), ranges from ~5 to 20 m along the array. The height is greatest in the transfer zone, and least along the northern main segment (Fig. 7c). Fold height is also greatest where displacement measured from fault scarps is least (Fig. 7c). Displacement calculated by conserving fold cross-sectional area varies between ~1 and 8 m with  $1\sigma$  error of ~1–2 m (Fig. 7d); about the same magnitude error as for individual fault scarps. Along-strike variation in displacement from folding follows a similar, though more subdued,

pattern as fold height. Greatest displacement occurs in the southern end of the transfer zone and decreases to the north. Because fold strain is converted to equivalent fault displacement, it can be directly compared and summed with displacement measured on fault scarps. Summed fault and fold displacements (Fig. 7d) are more constant along strike than the fault scarp displacements alone, i.e. fold displacement is generally greater where fault scarp displacement is less.

### 5.3. $D_{max}$ versus $L$ scaling

The maximum displacement and fault-trace length ( $D_{max}$  and  $L$ ) were surveyed along the two-dimensional surface trace of 37 fault segments along the OFZ. Both linear and power-law least-squares regressions provide good statistical descriptions of the  $D_{max}$ – $L$  relationship (Fig. 8): a linear regression (Fig. 8a) yields a slope of 0.01 ( $R^2=0.91$ ), whereas a power-law regression (Fig. 8b) yields a scaling exponent (Eq. (2)) of  $n=1.1$  ( $R^2=0.84$ ). A  $t$ -value (Clark and Cox, 1996) of 1.35 for the OFZ data indicates that the power-law scaling exponent is not statistically different from 1.0, i.e. linear scaling, at the 95% confidence level, a result that is consistent with theoretical modeling suggesting linear  $D_{max}$ – $L$  scaling for all modes of faulting (Cowie and Scholz, 1992b), but the possibility of non-linear scaling ( $n \geq 1$ ) cannot be eliminated.

In the case of the Ostler Fault, however, only ~20 ky of cumulative displacement is being measured, because that is the age of the deformed terrace surface that was surveyed. Given that fault initiation is much older than 20 ka and that many of the fault segments are likely to be significantly older than the surveyed terrace, the linear  $D_{max}$ – $L$  scaling may be fortuitous. Nonetheless, it is noteworthy that many of the Ostler Fault segments (those with displacements of >2–3 m) are likely to have ruptured multiple times since

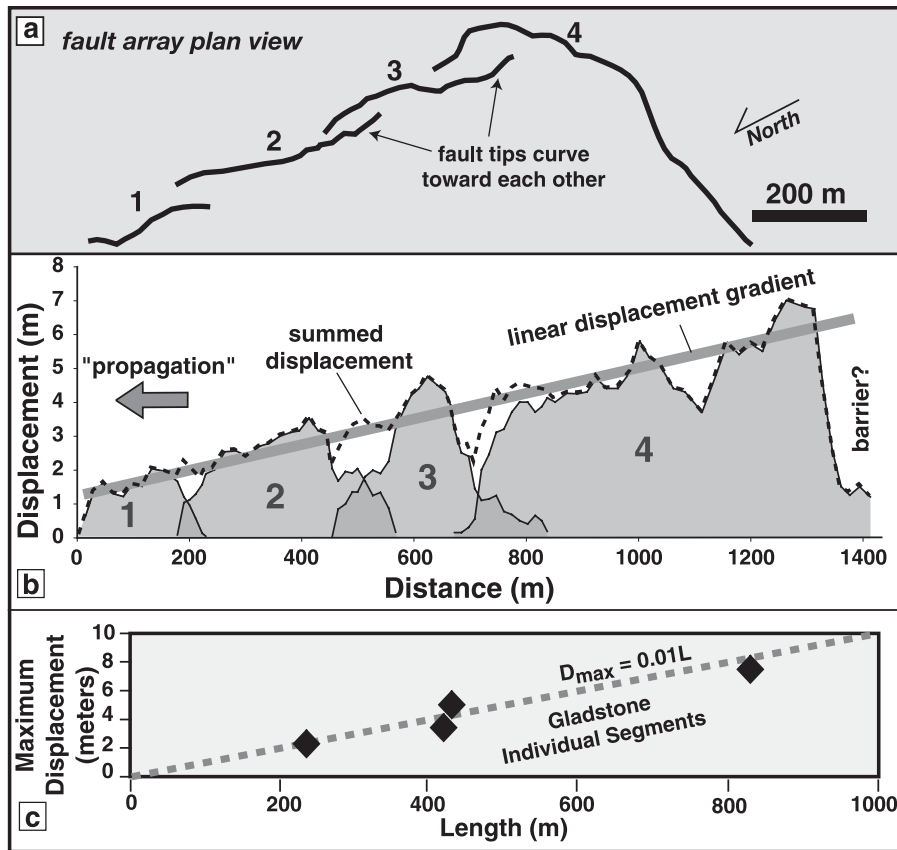


Fig. 6. The Gladstone fault array. (a) Fault trace map pattern reveals four east-stepping *en échelon* segments. In two overlap zones, fault tips wrap toward the adjacent fault segment, reminiscent of interacting crack behavior. (b) Displacement-length profiles on a common projection with their summed displacement reveal a smooth, linear displacement gradient along the array and a maximum displacement near the array's southern termination. Pattern suggests propagation to the north and perhaps a barrier to propagation in the south. (c) Maximum displacement and length of the four individual segment scarps of the array show self-similar scaling and define a relationship of  $D_{max} = 0.01L$ .

20 ka and that the entire ensemble of fault segments appears to scale uniformly.

Overall, maximum displacement and fault-trace length ( $D_{max}$  and  $L$ ) along the OFZ are positively correlated over almost two orders of magnitude (Fig. 8).  $D_{max}$  and  $L$  data from the Ostler Fault segments match scaling trends in the global dataset (Schlische et al., 1996) and actually fill in a mesoscale (20–2000 m) zone that was poorly represented by previous data (Fig. 9). Because most of the global compilation is expected to represent maximum displacement along entire fault zones, rather than maximum displacement on segments within a fault zone (as the Ostler data represent), the match of the Latest Quaternary displacements from the OFZ to the global data set may be fortuitous. Indeed, the maximum observed Late Quaternary displacement with respect to the entire OFZ (black box; Fig. 9) falls well outside the global data and may represent a transitional stage between co-seismic displacements and a mature, fully linked fault zone.

#### 5.4. Fault-size distribution

Analysis of fault-size dimension ( $L$  or  $D_{max}$ ) versus the

cumulative number of fault segments larger than that dimension reveals a power-law size distribution over a substantial range, with some deviation at relatively long and short fault segment lengths (Fig. 10). Fault segments in our two-dimensional analysis of the OFZ range from 31 to 1750 m in length and span nearly two orders of magnitude (Table 1). Generally, shorter fault segments are more numerous, with a decrease in frequency with increasing segment length (Fig. 10a). The linear part of the length distribution yields a well-defined scaling exponent (Eq. (1)) of  $C = 0.82$  ( $R^2 = 0.96$ ). Faults on the extremes of the length range (0–90 and 700–1750 m) deviate from the power-law regression line (Pickering et al., 1994). That is, fewer very long and very short faults were delineated than would be predicted by a power-law distribution with  $C = 0.82$ .

Cumulative size-frequency analysis of  $D_{max}$  data (Fig. 10b) reveals a power-law distribution similar to the length data. However, an abrupt break in slope occurs at  $\sim 1$  m. For faults with  $D_{max}$  less than  $\sim 1$  m, a  $C$  of 0.39 ( $R^2 = 0.98$ ) best fits the data, whereas for larger faults,  $C$  is 2.5 times greater at 1.05 ( $R^2 = 0.98$ ). Hence, in comparison with faults with displacements of  $< 1$  m, the frequency of increasingly larger offsets diminishes considerably more

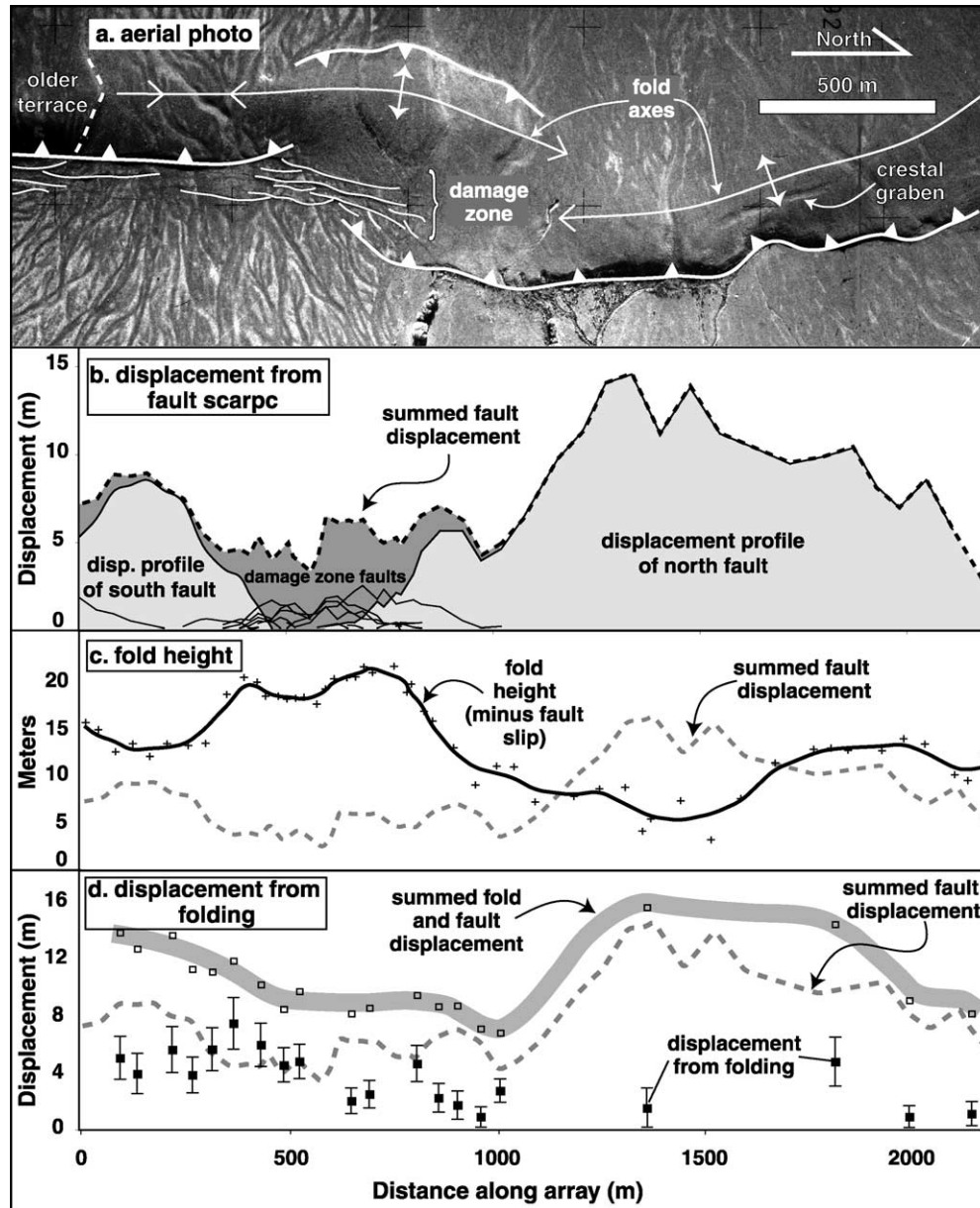


Fig. 7. The Benmore fault array. (a) Aerial photograph of the array. Two main segments terminate in an area of ‘damage zone’ faults, a backthrust, and folding. (b) Individual and summed (dotted line) displacement profiles on a common projection. Note that a displacement minimum occurs in the transfer zone between the two main segments. (c) Fold height along the array. Height is greatest in the transfer zone, where fault displacement is lowest. (d) Estimates for displacement on a  $50^\circ$  fault is based on fold cross-sectional area (solid squares) and sum of displacement from folding and fault scarps (open squares and gray line).

rapidly for offsets  $> 1$  m. Notably, most of the ‘damage zone’ faults, which are interpreted to represent juvenile faults that have experienced few ruptures, fall in the frequency domain with more limited ( $< 1$  m) displacement.

## 6. Discussion

### 6.1. Sources of uncertainty in the dataset

As in most other  $D_{\max}$ - $L$  datasets (Cowie and Scholz, 1992b; Gillespie et al., 1992; Schlische et al., 1996), data

from the OFZ exhibit considerable scatter. In some cases, for a similar  $L$ , the  $D_{\max}$  can vary by a factor of 2 or 3. Variability in the data results from both measurement uncertainty and natural scatter. Monte Carlo simulations indicate that poorly constrained fault dip contributes most ( $\sim 40\%$ ) to the  $D_{\max}$  measurement error. Uncertainty in the dip of displaced geomorphic surfaces typically accounts for  $\sim 35\%$  of the error, and uncertainties associated with GPS accuracy and topographic roughness are  $\sim 25\%$  of the error. Variable fault dip along strike is not accounted for and likely contributes additional error. We assume, for example, that the probability of fault dip follows a Gaussian

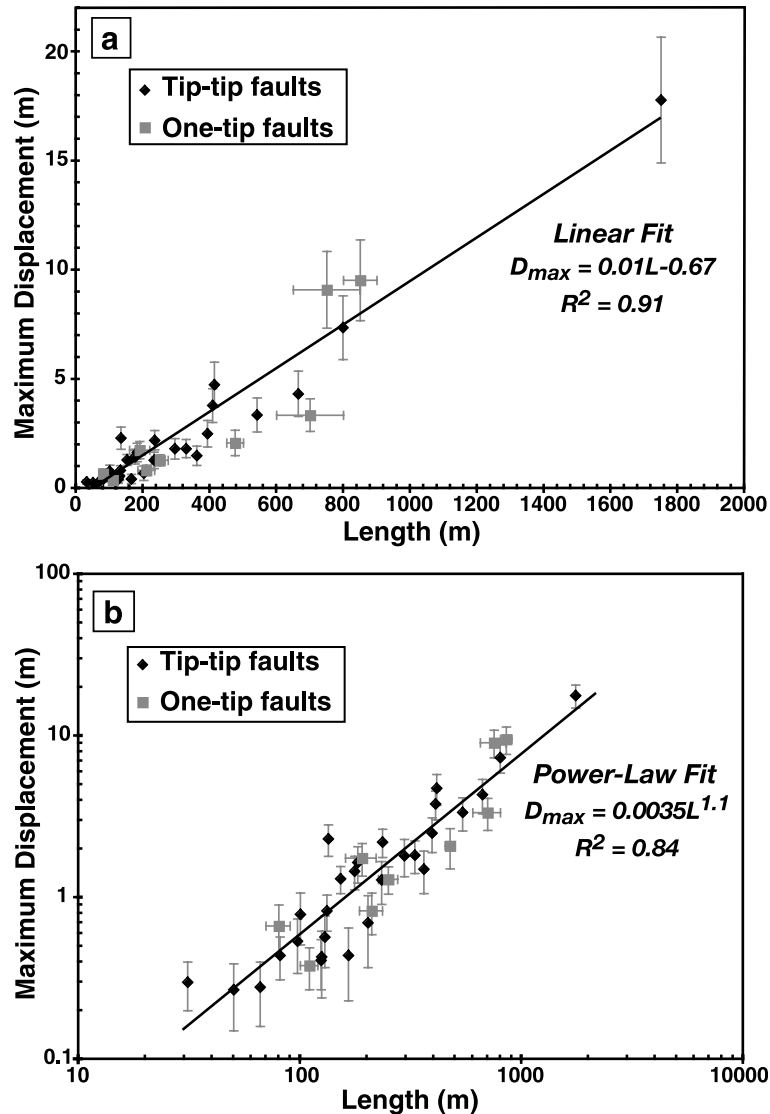


Fig. 8. Maximum displacement versus fault-segment length for the OFZ. (a) Linear  $D_{max}$  versus  $L$  plot with best-fit line of  $D_{max} = 0.01L - 0.67$ . Error bars for  $D_{max}$  are from Monte Carlo uncertainty estimates, and error bars for  $L$  are for one-tip fault segments where total length is extrapolated from the displacement-length profile. (b) Log-log plot of the same data, with a best-fit power-law curve of  $D_{max} = 0.0035L^{1.1}$ .

distribution about the same mean for all segments. If, however, the mean dip varied between segments, our estimates would not capture this uncertainty.

Natural variability also introduces scatter into the data. Variations in material properties are predicted to impact observed  $D_{max}/L$  ratios (Cowie and Scholz, 1992b). Although the bedrock beneath the fault is a single unit, the Torlesse Graywacke, the thickness and degree of induration of Quaternary gravels and underlying Tertiary strata varies, but in a poorly known manner, along the OFZ (Blick et al., 1989; Long et al., 2000). Variability in the shallow stratigraphy likely impacts the topographic expression of subsurface displacements. Similarly, although the regional remote tectonic stress field is probably uniform along the fault zone, segment interaction causes perturbations in the local stress field. Evidence for segment interaction in the OFZ can be seen in both the map patterns

(curving fault tips) and profiles showing displacement transfer between segments (e.g. Fig. 6). Fault-growth patterns resulting from segment linkage are also a likely source of scatter in the  $D_{max}-L$  data (Cartwright et al., 1995) (Fig. 11a). Because displacement distribution varies vertically on a fault plane, the structural level at which displacement is measured also affects the  $D_{max}/L$  ratio. Given that faults have propagated upward through Tertiary and Quaternary strata, maximum displacement on these faults is most likely at some depth below the surface (Suppe and Medwedeff, 1990; Wickham, 1995), yet the  $D_{max}-L$  profiles are measured at the surface (Fig. 1). Moreover, in the case of the OFZ, initiation of faulting in most places is very likely to predate creation of the  $\sim 20$  ka glacial outwash surface. Because creation of the strath surface bevels the bedrock and removes or obscures any prior offsets, the  $D_{max}$  measured on those surfaces is very likely to be an

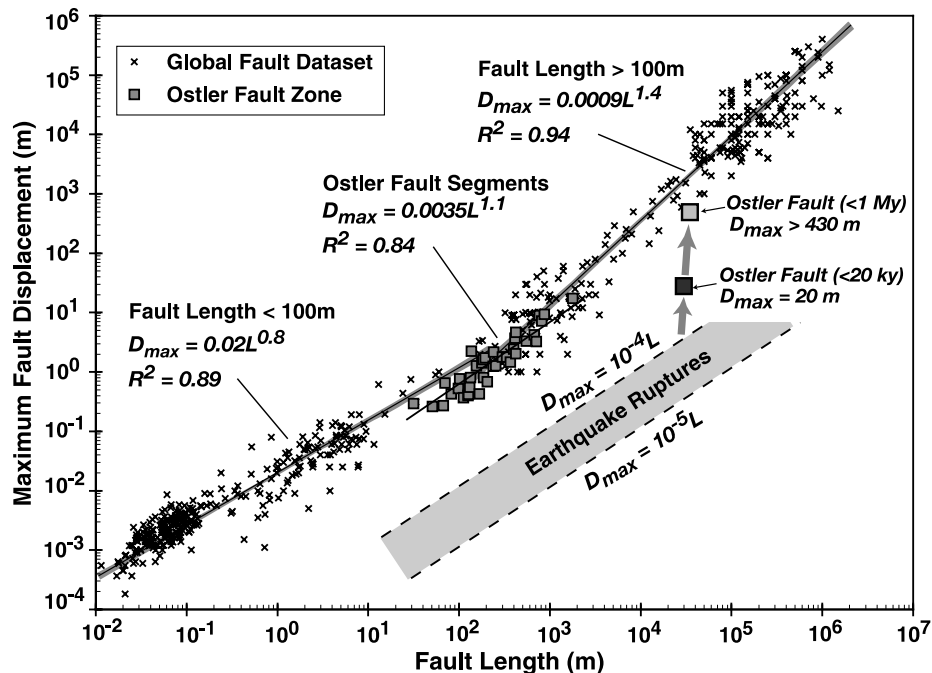


Fig. 9. Plot of maximum displacement and fault length for global fault dataset (Schlische et al., 1996) and fault segments of the Ostler fault zone. Maximum displacement versus rupture length for individual earthquakes fall within the range of  $D_{\max} = \sim 10^{-4} - 10^{-5}L$  (Scholz, 1982; Wells and Coppersmith, 1994). The measured segments of the OFZ represent displacement from  $\leq 6-10$  earthquakes on pre-existing fault segments, some of which probably achieved much of their length over many more earthquake cycles. Nonetheless, these data fall within the range of the global fault dataset, which samples mostly ancient faults that have accumulated displacement from many earthquakes, and not within the range of earthquake ruptures. The maximum accumulated post-20-ka displacement on the OFZ (black box on right) may represent a transition (arrows) from single seismic ruptures to that of faults that have accumulated displacement over many earthquakes. Power-law regressions (shaded areas show 95% confidence intervals) for faults  $> 100$  m and  $< 100$  m length suggest a change in scaling at  $L \sim 100$  m.

underestimate of the total accumulated displacement on the fault. Finally, fault ruptures in unconsolidated sediment may cause irregular surface offsets, because some displacement may be dissipated when the fault ruptures unconsolidated material (Bray et al., 1994). Given these many sources of uncertainty, the well-defined scaling characteristics are strikingly systematic.

## 6.2. Displacement profiles and transfer zones

### 6.2.1. Gladstone array

The Gladstone array summed displacement profile (Fig. 6) shows two striking features: (1) a smooth, linearly increasing displacement gradient that persists for most of the array's length, and (2) a highly asymmetric displacement maximum near the south end of the array. The smooth displacement gradient suggests that the four segments of the array are interacting and are likely to be kinematically or structurally linked. Linear displacement gradients, such as on the Gladstone array, have been observed in other fault systems (e.g. Peacock and Sanderson, 1996; Cowie and Shipton, 1998; Manighetti et al., 2001), and conceptual models (Walsh and Watterson, 1988; Peacock and Sanderson, 1996) suggest that summing the displacement profiles of propagating ruptures can produce linear displacement gradients.

Similar to the Gladstone array (Fig. 6), asymmetric displacement profiles in normal faults in Afar, East Africa, have been interpreted as a product of barriers to propagation of one fault tip and unimpeded propagation of the other tip (Manighetti et al., 2001). Barriers may be changes in material strength due to lithology or fracture density, or changes in local stress conditions from fault interaction (Nicol et al., 1996b; Manighetti et al., 2001). In the case of the Gladstone array, the displacement on the southern tip abruptly terminates near a large scarp that could be a cross-cutting fault segment, representing a barrier to propagation. This fault could also accommodate deformation as the Gladstone array decreases in displacement in the north.

Although the  $D_{\max}/L$  ratios for individual segments of the Gladstone array are close to 1% (Fig. 6c), if the entire array is considered as one fault, the  $D_{\max}/L$  ratio declines to 0.5% and lacks the self-similarity of the individual segments. Whereas this non-self-similarity could be interpreted as a result of recent fault linkage and abrupt lengthening of the total fault length (Cartwright et al., 1995; Mansfield and Cartwright, 2001), we argue that these fault segments were probably linked before the terrace surface that is displaced by them was created.

The tapered displacement gradient of the Gladstone array would usually be interpreted to be a product of ongoing fault propagation with lesser displacement towards the fault tip

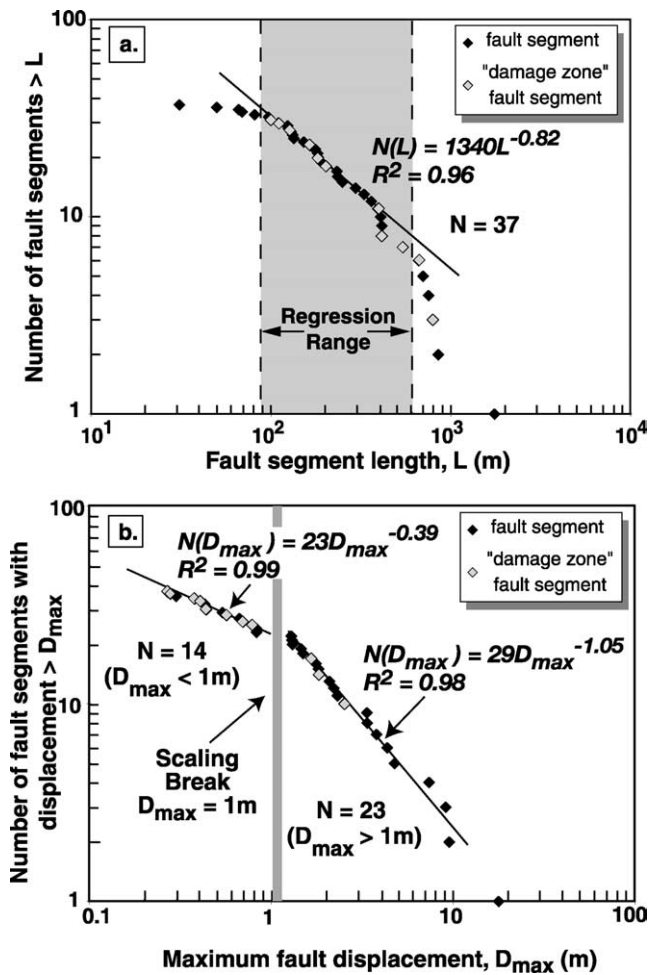


Fig. 10. Fault size–frequency distributions. (a) Fault-segment length versus cumulative number of fault segments longer than that length on a log–log scale. For fault segments 90–600 m in length, the data fit a power-law ( $C = 0.82$ ), indicating a self-similar size distribution. (b) Maximum fault-segment displacement. A similar power-law distribution is observed, but a distinct scaling break occurs at  $D_{max} \sim 1$  m. For fault segments with  $D_{max}$  larger than 1 m,  $C = 1.05$ , and for fault segments with  $D_{max}$  less than 1 m,  $C = 0.4$ .

(e.g. Manighetti et al., 2001 or Medwedeff, 1992). For the Gladstone array, however, the measured displacements record <20 ky of deformation (the age of the faulted terrace surface), and these fault segments are embedded in a larger, older fault zone. It seems unlikely that the fault tip

propagated over a kilometer in 20 ky. Consequently, the Gladstone displacement gradient is unlikely to be primarily a product of long-term tip propagation. Instead, we interpret it to represent part of a larger displacement transfer zone in which another fault strand that initiates  $\sim 2$  km west of the surveyed Gladstone array (Fig. 2) is likely to absorb increasing amounts of slip to the north (Fig. 11). Because that westerly strand does not cut continuous terrace surfaces, no record of displacement gradients along it is readily attainable to test this prediction.

The Gladstone array is noteworthy, therefore, because this linked array of fault segments have accumulated displacement as if it were a single fault within a slip-transfer zone: all the fault segments have essentially the same age with respect to the measured displacement; they have accumulated slip through multiple earthquakes; each fault segment scales in a self-similar and predictable style (Fig. 6c); and yet a persistent integrated slip gradient has been propagated along the array. This systematic gradient provides strong evidence that, despite the individual surface scarps and displacement profiles, these segments link in the subsurface to a common slip surface.

### 6.2.2. Benmore array

In the Benmore array, two large segments appear to be in the process of linking. Unlike in the Gladstone array, the mapped surface ruptures do not presently overlap at the surface. Although the region of non-overlap could represent a major displacement deficit, strain between the major fault traces is accommodated by a combination of ‘damage zone’ fault segments, a backthrust, and folding (Fig. 7). Strain on these intermediate structures appears insufficient, however, to form a completely smooth displacement transfer from one major fault strand to the other. Unlike the Gladstone array, a displacement minimum does occur between the main segments and may signify nascent or incomplete linkage (Dawers et al., 1993).

Fault-related folding is significant in the Benmore array. Fold height, which varies by a factor of four along the array, reaches its greatest height ( $\sim 20$  m) in the transfer zone (Fig. 7), and decreases as the fold plunges to the north, suggesting that lower displacements recorded on fault

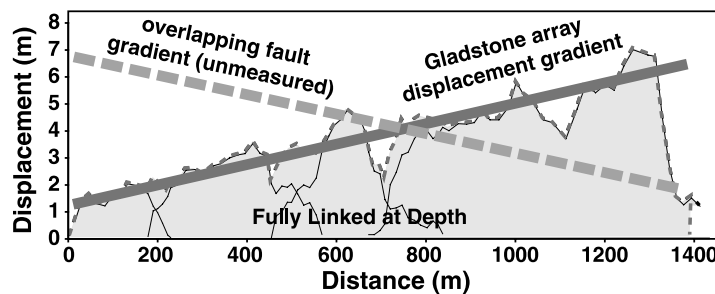


Fig. 11. Self-similarly scaled, but fully linked (at depth) segments of the Gladstone array display a coherent gradient due to a trade-off with a nearby fault whose displacement gradient increases in the opposite direction. In this interpretation, decreasing displacement toward the north is not indicative of significant tip propagation over the time interval ( $\sim 20$  ky) that encompasses the measured slip displacement. Compare with Fig. 6b.

Table 1  
Fault length and maximum displacement for segments of the OFZ

Location	Fault number	$D_{\max}$ (m)	$D_{\max}$ $1\sigma$ error (m)	Trace length (m)	Estimated $L^a$ (m)
Benmore	BM 1	1.82	0.47	295	80
	BM 2	0.67	0.23	69	
	BM 3	0.43	0.19	125	
	BM 5	0.44	0.13	81	250
	BM 6	1.3	0.25	219	
	BM 7	0.7	0.33	202	
	BM 8	0.83	0.21	132	
	BM 9	2.09	0.58	498	
	BM 10	0.79	0.28	100	
	BM 12	1.5	0.44	361	
	BM 20	17.8	2.88	1750	750
	BM 21	1.83	0.42	329	
	BM 22	9.1	1.76	524	
	BM 30	0.41	0.14	124	
	BM 31	1.76	0.4	153	190
	BM 31b	0.3	0.1	31	
	BM 32	0.83	0.24	183	210
	BM 33	0.57	0.2	129	
	BM 34	0.27	0.12	50	110
	BM 35	0.44	0.21	165	
BM 36	0.38	0.11	99		
BM 37	0.28	0.12	66		
BM PL 1	3.37	0.78	541		
BM PL 2	2.51	0.61	393		
Dart's Bush	DB 1	4.34	1.04	664	
	DB 2	1.29	0.38	233	
	DB 3	1.46	0.34	176	
Gladstone	GL 1	1.65	0.42	182	
	GL 2	0.54	0.2	97	
	GL 3	1.31	0.25	152	
	GL 4	2.31	0.51	134	
	GL 5	2.21	0.44	235	
	GL 6	3.8	0.77	408	
	GL 7	4.76	1.03	413	
	GL 8	7.37	1.46	798	
	GL 9	3.36	0.75	426	
Top MacMillan	TM 1	9.54	9.54	715	850

<sup>a</sup> Fault trace length of segments where one tip covered is extrapolated from the displacement profile (one-tip faults).

scarps in the transfer zone are compensated for by greater fold strain (Nicol et al., 2002). This result appears to contradict traditional models of fault-related folding, in which fold magnitude increases as slip accumulates on a fault (Suppe and Medwedeff, 1990). The presence of a major segment boundary, however, may generate high stress conditions that lead to increased fold amplitude in the transfer zone as a way to maintain relatively constant strain along the fault system (Nicol et al., 2002). Estimates of displacement from fold cross-sectional areas show a less direct relationship to fault displacement than fold height, but still tend to be highest ( $\sim 8$  m) in the transfer zone and decrease to the north. Summed fold and fault displacements produce an along-strike profile with a more subdued displacement minimum than that observed for faulting alone. Although the folding at Benmore may not fully compensate for the slip deficit between fault segments, the major role of folding in absorbing strain clearly indicates the importance of off-fault strain in contractional fault zones.

As opposed to the Gladstone array, the major faults in the Benmore array are likely to be actively propagating towards or past each other, as is apparent from the growing folds above the southerly fault tip, as well as the observed slip deficit in between the fault tips. Whereas the surveyed displacements in both arrays represent slip in the past 20 ky, the Gladstone array is likely to be exploiting fault segments that existed before the terrace formed, whereas the Benmore array is likely to incorporate juvenile faults that are compensating for the slip deficit between the propagating fault tips.

### 6.2.3. Large-scale and long-term displacement profile

Tertiary strata in the MacKenzie Basin are exposed as hanging wall uplifts that provide the oldest exposed record of displacement on the OFZ. These uplifts, on a scale an order of magnitude larger than the faults described thus far, define a  $D_{\max}/L$  ratio and displacement profile generally similar to that of individual segments (Fig. 12). Topographic profiles were extracted from a 10-m TOPSAR DEM. The

hanging wall profile follows the crest of the uplifted, west-tilted Tertiary strata. Surfaces of back-tilted Quaternary terraces can be traced or project to near the range crest, whereas the footwall profile runs along the Quaternary alluvial surface that has aggraded above any underlying Tertiary strata. When plotted together, these profiles define the observable relief across the fault (Fig. 12). Relief represents a minimum estimate of vertical displacement, because erosion may have lowered the uplifted crest and deposition of unknown thickness has certainly occurred in the footwall. Nonetheless, the summits of the hanging wall uplifts define a quasi-elliptical profile similar to that observed in segments of the OFZ and numerous other faults (e.g. Dawers and Anders, 1995; Schlische et al., 1996; Manighetti et al., 2001).

The 37-km-long southern section of the OFZ has a relief of  $\sim 430$  m, which, when a  $50^\circ$  fault dip is assumed, gives a minimum  $D_{\max}/L$  ratio of 1.5% (Fig. 9). This is  $\sim 50\%$  larger than the  $D_{\max}/L$  ratio of  $\sim 1\%$  calculated here for segments of the OFZ (Fig. 8). Recall, however, that 1% is a low estimate because of the young ( $\sim 20$  ka) surfaces on which segment displacement was measured. This large-scale view of the OFZ nonetheless appears to illustrate striking self-similarity, both in profile shape and  $D_{\max}/L$  ratio (Fig. 12c), between the entire fault zone and its constituent segments (Dawers and Anders, 1995).

The age of fault initiation can be estimated in two ways. Extrapolation to the  $\sim 0.75$  mm/yr uplift rate calculated for younger surfaces of the OFZ predicts fault initiation at  $\sim 600$  ka. Displacement scaling in earthquakes suggests a 35-km-long rupture should produce vertical displacements of 0.5–1.5 m (Scholz, 1982; Wells and Coppersmith, 1994). Assuming an earthquake recurrence interval of  $\sim 3$  ky (Van Disen et al., 1993),  $\sim 400$  m of uplift would occur in 800–2400 ky.

### 6.3. Fault-size distribution

$D_{\max}$  and  $L$  cumulative size–frequency distributions (Fig. 10) are power-law for much of their range and have  $C$ -values similar to those calculated from fault maps and predicted numerical models (Cowie et al., 1995; Cladouhos and Marrett, 1996). The length–frequency distribution (Fig. 10a), however, deviates from the power-law prediction at short and long fault lengths, a characteristic of several datasets of natural fault systems. Incomplete sampling is often invoked to explain the deviations (e.g. Pickering et al., 1994). For small faults ( $< 100$  m), resolving the scarps and fault terminations on the outwash surface becomes difficult as displacements approach the same magnitude as the topographic roughness. Therefore, small-displacement ( $< 30$  cm) faults are undersampled. Longer faults ( $> 500$  m) are incompletely sampled because they are more likely to be obscured by hanging wall erosion, to intersect the boundaries of the sample area, or to cut surfaces of several ages.

Nicol et al. (1996a) suggest that some deviation from power-law cumulative size–frequency distributions may be

real and attributable to control by different processes at different scales. The  $D_{\max}$  data from the OFZ (Fig. 10b) can be interpreted as having two distinct power-law distributions with a break in scaling at  $D_{\max} \sim 1$  m. Most faults with  $D_{\max}$  less than 1 m are from the population of ‘damage zone’ segments in the Benmore linkage zone (Fig. 10b), and it is possible that these segments operate under different scaling than the main fault strands. In particular, these faults may represent juvenile faults that have ruptured in only one or two earthquakes. As such, these damage zone faults might be considered more analogous to the isolated faults measured in other  $D_{\max}$ – $L$  studies (Dawers et al., 1993). The fact that the scaling decreases abruptly when  $D_{\max} > 1$  m (Fig. 10b) could result from fault linkage and lengthening without commensurate displacement increases: the frequency of large displacement faults is reduced due to amalgamation, rather than simple lengthening, of smaller faults (Cartwright et al., 1995; Gupta and Scholz, 2000).

### 6.4. $D_{\max}$ – $L$ scaling

An important goal of this study is to define the  $D_{\max}$ – $L$  relationship for segments of the OFZ and to determine if scaling relations for thrust faults are similar to those of normal faults. The linear or power-law nature of the  $D_{\max}$ – $L$  relationship has been a source of debate and uncertainty (e.g. Walsh and Watterson, 1988; Cowie and Scholz, 1992b; Gillespie et al., 1992). Modeling based on elastic–plastic fracture mechanics (Cowie and Scholz, 1992a) predicts linear scaling with a constant of proportionality dependent on rock type and tectonic environment. Cowie and Scholz (1992b) also reviewed natural fault data (almost all from normal faults) and concluded that most individual datasets are best fit by a linear relationship. For the OFZ, both linear and power-law relationships are statistically admissible.

The  $D_{\max}/L$  ratio,  $k$  (Eq. (2)) of fault segments of the OFZ is 0.9% lower than similar normal fault datasets (Dawers and Anders, 1995,  $k = 1$ –2%; Manighetti et al., 2001,  $k = 1.5\%$ ) and much lower than Elliott’s (1976) dataset of thrust faults in the Canadian Rockies, which gives a  $D_{\max}/L$  ratio of 7%. Natural data scatter and variability in material and tectonic properties surely exist, but a more likely cause of the lower  $D_{\max}/L$  ratios in the OFZ is the young age of the surveyed geomorphic marker surfaces. Fault segments that displace the bedrock almost certainly pre-date the geomorphic surfaces on which displacements were measured, but any record of older displacement would have been eroded away during the generation of the surfaces. Thus, despite a pristine terrace surface at  $\sim 20$  ka, Quaternary fault segments in the OFZ would have already offset the underlying bedrock. Once the terrace was formed, each successive earthquake rupture should break all or part of the pre-existing fault surface and rupture to the terrace top. Therefore, our measurements of segment length probably approach the true maximum fault length, but only account for slip since the abandonment of this latest Quaternary

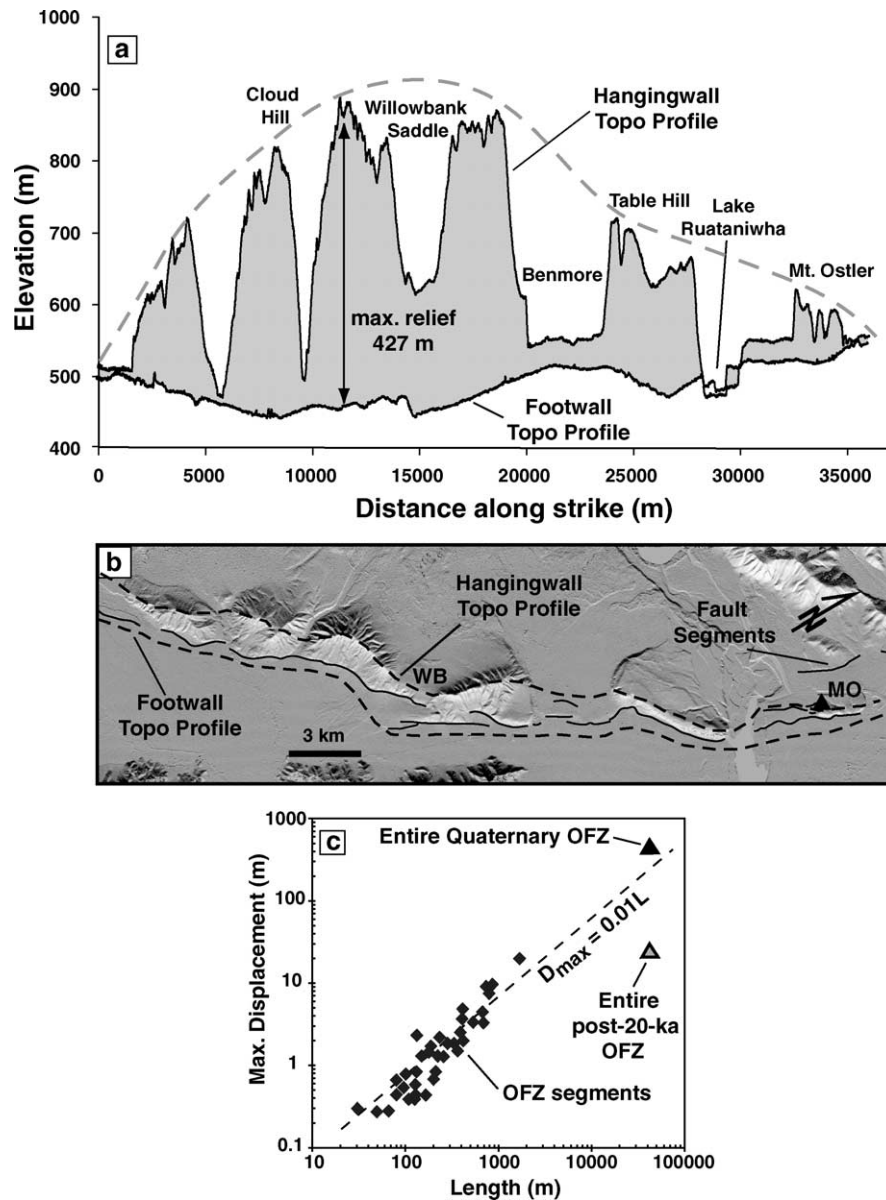


Fig. 12. Large-scale displacement profile of the OFZ. (a) Topographic profiles of the hanging wall and footwall of the southern portion of the OFZ. Hanging wall profile along the topographic crest of uplifts west of the fault. The high points of the uplifts can be connected to form a quasi-elliptical profile similar to profiles of individual segments. (b) Profiles extracted from 10-m DEM. MO: Mt Ostler; WB: Willowbank Saddle. The profile has a length of  $\sim 37$  km and a maximum relief of  $\sim 430$  m. (c) Plot of maximum displacement versus length for segments of the OFZ and for the entire southern portion (from Panel a). Note that the large-scale profile, like individual segments, could fit a  $D_{max}/L$  ratio of 0.01, indicating a self-similarity between segments and entire fault.

terrace surface. This likely yields a considerable underestimate of the actual  $D_{max}/L$  ratio over the lifetime of the fault segment and may account for discrepancies between the OFZ segment data and other fault datasets (Fig. 9). Specifically, the segment data would be expected to plot to the right of the global dataset.

Despite the caveats above, it is striking that self-similar scaling exists for these fault segments. Possibly every segment has been systematically accumulating displacement in each rupture at a scale proportional to its length. It seems likely, however, that some of the damage zone faults are young structures related to incipient linkage between

larger, propagating fault segment tips. These faults segments are expected to be lengthening proportionally more rapidly than the previously established fault segments. Whereas the youngest damage zone ruptures have probably only slipped in 1–2 earthquakes, larger and longer fault segments are likely to have experienced 6–8 earthquakes since the terrace was created.

In the Ostler system, the presently observed length of fault segments is interpreted to have been established early following terrace abandonment (i.e. in a single rupture, because the fault was already well established in the shallow subsurface). Without much fault lengthening in subsequent

ruptures, slip continues to accrue along the fault segments, while shortening in transfer zones occurs by other mechanisms, such as small-scale faulting, folding, and backthrusting. The isolated and overlapping fault scarps at the surface are likely to be kinematically linked with a continuous fault system at depth. Segment boundaries are likely to be defined early during upward propagation of the Ostler fault through a heterogeneous three-dimensional stress field (Mandl, 1987; Walsh et al., 2003). Such a model would produce non-self-similar growth as segment length grows initially very rapidly and then abruptly slows, while displacement changes systematically and gradually catches up. The changing  $D_{\max}/L$  ratios that we document for varying spatial and temporal scales in the OFZ support also suggest a non-self-similar fault growth history (Fig. 9) (Gupta and Scholz, 2000; Walsh et al., 2002).

In the OFZ, four different  $D_{\max}/L$  ratios have been observed: first, for fault segments with no more than 20 ky of slip accumulation, a ratio of  $\sim 1\%$  pertains (Fig. 8); second, for a linked fault array with a length of  $\sim 1.4$  km (Fig. 6), a ratio of 0.5% is apparent for slip since 20 ka; third, for an array of 37 km length, the  $D_{\max}/L$  ratio is  $< 0.1\%$  over the same 20 ky interval (Fig. 9); and fourth, when the entire recorded life of the fault is considered, accumulated slip is at least 1.5% of the fault length (Fig. 12). These differing ratios offer support both for the model of Cartwright et al. (1995) in which fault linkage drives  $D/L$  ratios away from the linear trend of individual faults and for a change in scaling ratio as faults lengthen past some threshold (Fig. 9). In addition, these ratios suggest that, with respect to the accumulated displacement, shorter faults can lengthen relatively faster than longer faults. This may reflect either the lower likelihood of linking larger faults or changes in the ways faults propagate and accumulate slip when they achieve lengths equal to or exceeding the thickness of the brittle crust. Finally, observed  $D_{\max}/L$  ratios range over an order of magnitude depending on whether individual or linked fault segments are considered and whether cumulative displacement is measured since fault initiation or only since a geomorphic marker was created. Not only does this suggest that caution must be used when comparing datasets from different populations of faults, but those data that appear as outliers with respect to typical  $D_{\max}/L$  ratios may be recording transitional stages between the coseismic rupture-displacement scale and the fully linked, mature fault stage (Figs. 9 and 11).

An implication of the modeling of Cowie and Scholz (1992a) is that faulting from different stress regimes and lithological settings will have different  $D_{\max}-L$  scaling, because the parameters for shear strength and shear modulus of the surrounding rock, frictional shear stress on the fault, and ratio of remote stress loading to rock shear strength all affect the  $D_{\max}-L$  relationship. Nevertheless, the global fault dataset (Schlische et al., 1996) shows a clear positive trend over nine orders of magnitude (Fig. 9). These data comprise faults that have accumulated slip from many earthquakes,

and most of the data come from inactive faults. Wells and Coppersmith (1994) and Scholz (1982) have compiled data on the length and displacement of earthquake ruptures that define a positive linear relationship between  $D_{\max}$  and  $L$  with a  $D_{\max}/L$  ratio of  $\sim 2-5 \times 10^{-5}$ . Individual segments of the OFZ, which record displacement of only the last  $\sim 20$  ka, fall clearly within the range of the global fault dataset, and have  $D_{\max}/L$  ratios ( $\sim 0.01$ ) at least two orders of magnitude greater than those of earthquake ruptures.

A change in slope in the global fault data at  $L \sim 100$  m is apparent (Fig. 9). Shorter faults best fit the power-law relationship  $D_{\max} = 0.02L^{0.8}$ , whereas faults longer than 100 m best fit  $D_{\max} = 0.0009L^{1.4}$ . Although Cowie and Scholz (1992b) argued that faults from different tectonic and lithologic settings have different  $k$ -values (Eq. (2)), and should not be combined, this scaling break persists in data that are synthesized from many settings and should, therefore, smooth site-specific differences. The OFZ data for fault segments straddle this scaling break and have an  $n$ -value of  $\sim 1.1$ , which is intermediate between  $L > 100$  and  $< 100$  regressions for the global dataset (Fig. 9). This break in slope implies that the mechanics of fault ruptures may vary for small ( $10^{-2}$ – $10^2$  m long) faults versus those  $> 10^3$ – $10^4$  m long. The physical basis for such variation, if it exists, needs to be explored.

#### 6.5. Segmentation and $D_{\max}-L$ scaling on the OFZ

Fault segments of the OFZ have  $D_{\max}/L$  ratios similar to those of ancient faults, not of earthquake ruptures (Fig. 9). The long-term scaling, however, can be understood in terms of linkage among fault segments and superposition of successive earthquakes, each with  $D_{\max}/L$  ratios much lower than those of mature faults. The largest surveyed displacements (15–25 m) on the last glacial surfaces are undoubtedly the product of multiple earthquake ruptures. Earthquake scaling relationships (Scholz, 1982; Wells and Coppersmith, 1994) predict maximum displacements of 1–2.5 m for a 50-km-long fault such as the OFZ. These predictions are generally compatible with the  $\sim 3$  m observed co-seismic displacements on the OFZ (Van Dissen et al., 1993). Based on a  $\sim 3$  ky earthquake recurrence interval (Van Dissen et al., 1993), perhaps 6–8 earthquakes have occurred since the abandonment of the  $\sim 20$  ka outwash surface. If each earthquake ruptures the entire length of the OFZ, 6–8 earthquakes should produce 6–20 m of displacement, a prediction that agrees well with field observations. Although the overall displacement on the surface can be explained by multiple earthquake ruptures with  $D_{\max}/L$  ratios of  $2-5 \times 10^{-5}$ , individual segments have much higher  $D_{\max}/L$  ratios. This discrepancy could be resolved if the entire fault ruptures along a single surface at depth, but splays into multiple segments within the overlying basin strata (Fig. 13) (Bray et al., 1994).

Seismic reflection data (Long et al., 2000) and field observations indicate that the MacKenzie Basin stratigraphy

consists of 10–100 m of Quaternary glacial outwash deposits and up to 800 m of Tertiary sediments (Glentanner Fm.) overlying a basement of Torlesse meta-sedimentary rocks. Although some of the regional scale segmentation may be rooted in the bedrock, we suggest that most segmentation in this study is a product of rupturing through Cenozoic basin stratigraphy (upper ~1000 m). Near its northern termination, the fault cuts bedrock at the surface, and a single, straight, and unsegmented fault scarp is present. In contrast, in addition to folding, parallel, en échelon, and ‘damage zone’ fault segments occur in that part of the OFZ underlain by Cenozoic strata. Presumably the sum of displacement on these structures equals the displacement of the underlying main fault strand in bedrock. Where we have observations (i.e. Benmore and Mt Ostler areas; Fig. 2), the total displacement of the 20 ka terrace across the entire fault zone is of the order of 15–25 m. Where fewer fault segments are present, displacements are greater on the individual faults. The compensation or displacement transfer that we observe at the ~500 m scale at Benmore (Fig. 7) also occurs in multiple faults at the ~3 km scale near Mt Ostler (Fig. 2a and c).

## 7. Summary and conclusions

Displacement and length of ~40 segments of the OFZ, New Zealand, were measured and analyzed in the first systematic study of along-strike displacement on mesoscale thrust faults. Deformation in this segmented, east-vergent fault zone is expressed as fault scarps and folds on a pristine ~20 ka glacial outwash surface, as well as older, dissected and uplifted surfaces on the hanging wall. Our data and analyses support the following conclusions:

1. Fault-displacement profiles display elliptical, box-like and linear displacement gradients. Fault segments are organized into arrays in which displacement is transferred between segment boundaries by either overlapping segments or damage-zone faults between segments. Displacement appears to be smoothly transferred between segments when substantial overlap exists for adjacent fault tips. Where linkage is incomplete, or segments do not overlap, a displacement minimum occurs in the transfer zone between major segments.
2. In contractional fault systems, folding may play an important role in accumulating displacement. Folding accounts for up to two-thirds of the total strain in some areas of the OFZ. Where documented in more detail in this study, fold height and displacement from folding are generally highest where the displacement measured from fault scarps is lowest, suggesting that folding and faulting are complementary deformation mechanisms that act to accommodate strain along the thrust system.
3. Where fault tips are propagating toward each other, but have not linked up, a deficit in total displacement may

occur between the fault tips. When faults or fault segments are linked (in either the subsurface or at the surface), smoother displacement gradients develop between the fault segments.

4. The mechanical stratigraphy of the MacKenzie Basin affects fault-trace patterns of the OFZ. Where basin fill is minimal, such as in the far northern part of the OFZ, the fault trace is a single linear feature. Where basin fill is thicker, in the central part of the fault zone, multiple fault segments form complex arrays. These segments are interpreted as splays within the Tertiary and Quaternary sediments that emanate from a singular rupture in the bedrock.
5. Cumulative size–frequency scaling in thrust-fault systems follows a power-law relationship consistent with both predictions of numerical models and normal fault populations. Fault trace length data deviates from a power-law relationship at the extremes of the size range, an effect that is likely due to sampling biases.  $D_{\max}$  data shows a change in the scaling exponent,  $C$ , at ~1 m that may be due to sampling effects or may reflect a different scaling relationship for small ( $D_{\max} < 1$  m) splays confined to the uppermost basin sediments.
6. Spanning over almost two orders of magnitude, the relationship between  $D_{\max}$  and  $L$  measured along the OFZ in two-dimensional surveys of fault segments is best described as linear with a slope of 0.009. This value is similar to several datasets for ancient, mostly normal-slip faults, but much larger than the  $D_{\max}/L$  ratio for earthquake ruptures ( $2\text{--}5 \times 10^{-5}$ ). Whereas length of earthquake ruptures is often measured as the total length of the ruptured region (Wells and Coppersmith, 1994), individual fault segments were surveyed here; this may

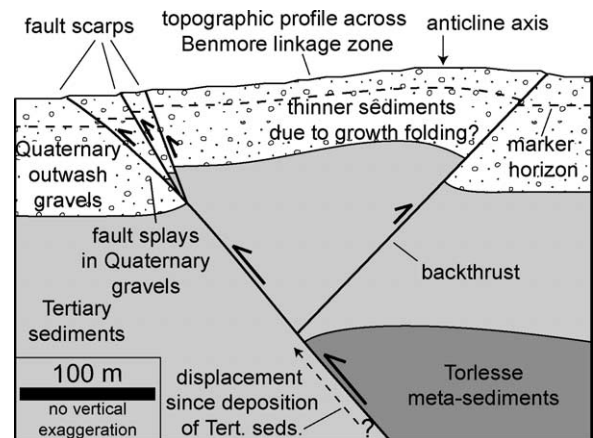


Fig. 13. Schematic 1:1 cross-section illustrating possible fault geometry in the Benmore area. GPS topographic profile shows five fault scarps and a broad hanging wall fold. Together, these structures record deformation over age of the surface (~20 ka). Splays likely occur in the upper layer of poorly indurated Quaternary outwash gravels, and the sum of displacement on these splays, backthrust and folding should equal the slip on a single underlying fault strand. Below the Quaternary gravels, up to 800 m of Tertiary Glentanner Fm. overlie Torlesse meta-sedimentary basement (Long et al., 2000).

account for some of the discrepancy. Segments of the OFZ follow similar scaling relationships to faults with sizes ranging across nine orders of magnitude and from all modes of faulting. Calculated  $D_{\max}$  values in the Ostler system are likely to be an underestimate because displacement is only recorded on fault scarps for the  $\sim 20$  ky since formation of the outwash surfaces that were subsequently faulted.

7. At the scale of the entire Ostler Fault system, the  $D_{\max}/L$  ratios define two extremes. Since 20 ka, the entire system  $D_{\max}/L$  ratio is  $<0.001$ , whereas the ratio is  $\geq 0.015$  since the fault zone was initiated. The former value falls below the typically observed  $D_{\max}/L$  ratios and appears to capture some of the transition from the displacement scale of coseismic ruptures to that of mature fault zones. The latter value is typical of the global data set for (predominantly normal) faults, but is much lower than the 0.07 ratio for large thrust faults in the Canadian Rockies. More data are needed on large thrust-fault systems to define their displacement scaling behavior (Elliott, 1976).
8. The OFZ accommodates up to 7% of plate convergence east of the Alpine fault, making it a significant structure in the eastern Southern Alps. Deformation on the OFZ likely originated before 600 ka, based on (i) extrapolation of recent uplift rates to the highest preserved uplifts, and (ii) extrapolation of earthquake-rupture scaling ratios and earthquake recurrence intervals.

## Acknowledgements

Haikai Tane of the Center for Catchment Ecology in Twizel, NZ provided assistance in the field, and high-resolution topographic data and aerial photography. The TOPSAR DEM used in this study was kindly supplied by NASA. This research was funded by National Science Foundation grant EAR-0117242. The manuscript was substantially improved by the incisive reviews of N. Dawers and A. Nicol.

## References

- Blick, G.H., Read, S.A.L., Hall, P.T., 1989. Deformation monitoring of the Ostler fault zone, South Island, New Zealand. *Tectonophysics* 167, 329–339.
- Bray, J.D., Seed, R.B., Cluff, L.S., Seed, H.B., 1994. Earthquake rupture propagation through soil. *Journal of Geotechnical Engineering* 120, 543–561.
- Cartwright, J.A., Trudgill, B.D., Mansfield, C.S., 1995. Fault growth by segment linkage; an explanation for scatter in maximum displacement and trace length data from the Canyonlands Grabens of SE Utah. *Journal of Structural Geology* 17, 1319–1326.
- Childs, C., Watterson, J., Walsh, J.J., 1995. Fault overlap zones within developing normal fault systems. *Journal of the Geological Society of London* 152, 535–549.
- Cladouhos, T.T., Marrett, R., 1996. Are fault growth and linkage models consistent with power-law distributions of fault lengths. *Journal of Structural Geology* 18, 281–293.
- Clark, R.M., Cox, S.J.D., 1996. A modern regression approach to determining fault displacement–length scaling relationships. *Journal of Structural Geology* 18, 147–152.
- Cowie, P.A., Scholz, C.H., 1992a. Physical explanation for the displacement–length relationship of faults using a post-yield fracture mechanics model. *Journal of Structural Geology* 14, 1133–1148.
- Cowie, P.A., Scholz, C., 1992b. Displacement–length scaling relationship for faults: data synthesis and discussion. *Journal of Structural Geology* 14, 1149–1156.
- Cowie, P.A., Shipton, Z., 1998. Quasistatic fault slip as an explanation for finite displacement gradients at fault tips. *Journal of Structural Geology* 20, 983–997.
- Cowie, P.A., Sornette, D., Vanneste, C., 1995. Multifractal scaling properties of a growing fault population. *Geophysical Journal International* 122, 457–469.
- Crider, J.G., Pollard, D.D., 1998. Fault linkage: three-dimensional mechanical interaction between echelon normal faults. *Journal of Geophysical Research, B, Solid Earth and Planets* 103, 24373–24391.
- Dawers, N.H., Anders, M.H., 1995. Displacement–length scaling and fault linkage. *Journal of Structural Geology* 17, 607–614.
- Dawers, N.H., Anders, M.H., Scholz, C.H., 1993. Growth of normal faults: displacement–length scaling. *Geology* 21, 1107–1110.
- DeMets, C., Gordon, R.G., Argus, D.F., Stein, S., 1994. Effect of recent revisions to the geomagnetic reversal time scale on estimates of current plate motions. *Geophysical Research Letters* 21, 2191–2194.
- Elliott, D., 1976. The energy balance and deformation mechanisms of thrust sheets. *Philosophical Transactions of the Royal Society of London* 283, 289–312.
- Gillespie, P.A., Walsh, J.J., Watterson, J., 1992. Limitations of dimension and displacement data from single faults and the consequences for data analysis and interpretation. *Journal of Structural Geology* 14, 1157–1172.
- Gupta, A., Scholz, C., 1998. Utility of elastic model in predicting fault displacement fields. *Journal of Geophysical Research* 103, 823–834.
- Gupta, A., Scholz, C., 2000. A model of normal fault interaction based on observations and theory. *Journal of Structural Geology* 22, 865–879.
- Long, D., Cox, S.J.D., Bannister, S., Gerstenberger, M., Yu, J.Z., Henrys, S.A., Okaya, D., 2000. Unveiling the secrets of the Mackenzie Basin: results from the 1998 SIGHT seismic reflection experiment. In: GSNZ/NZGS Joint Meeting: Geological Society of New Zealand Miscellaneous Publication 108A, 94pp.
- Mandl, G., 1987. Discontinuous fault zones. *Journal of Structural Geology* 9, 105–110.
- Manighetti, I., King, G.C.P., Gaudemer, Y., Scholz, C., Doubre, C., 2001. Slip accumulation and lateral propagation of active normal faults in Afar. *Journal of Geophysical Research* 106, 13667–13696.
- Mansfield, C.S., Cartwright, J.A., 2001. Fault growth by linkage: observations and implications from analogue models. *Journal of Structural Geology* 23, 745–763.
- Medwedeff, D.A., 1992. Geometry and kinematics of an active, laterally propagating wedge thrust, Wheeler Ridge, California. In: Mitra, S., Fisher, G.W. (Eds.), *Structural Geology of Fold and Thrust Belts*. Johns Hopkins University Press, Baltimore, MD, pp. 3–28.
- Nicol, A., Walsh, J.J., Watterson, J., Gillespie, P.A., Wojtal, S.F., 1996a. Fault size distributions; are they really power-law? *Journal of Structural Geology* 18, 191–197.
- Nicol, A., Watterson, J., Walsh, J.J., Childs, C., 1996b. The shapes, major axis orientations and displacement patterns of fault surfaces. *Journal of Structural Geology* 18, 235–248.
- Nicol, A., Gillespie, P.A., Childs, C., Walsh, J.J., 2002. Relay zones between mesoscopic thrust faults in layered sedimentary sequences. *Journal of Structural Geology* 24, 709–727.
- Nobes, D.C., Wallace, S., Davis, K.J., White, A., Burbank, D.W., 2003. Three-dimensional imaging of the Benmore segment of the Ostler Fault

- using ground-penetrating radar (GPR), resistivity tomography and differential GPS. In: Abstracts of the Australasian Quaternary Association and New Zealand Friends of the Pleistocene Conference, Westport, New Zealand.
- Norris, R.J., Cooper, A.F., 2001. Late Quaternary slip rates and slip partitioning on the Alpine Fault, New Zealand. *Journal of Structural Geology* 23, 507–520.
- Oncel, A.O., Wilson, T.H., Nishizawa, O., 2001. Size scaling relationships in the active fault networks of Japan and their correlation with Gutenberg–Richter *b* values. *Journal of Geophysical Research—Solid Earth* 106, 21827–21841.
- Peacock, D.C.P., Sanderson, D.J., 1991. Displacement, segment linkage and relay ramps in normal fault zones. *Journal of Structural Geology* 13, 721–733.
- Peacock, D.C.P., Sanderson, D.J., 1996. Effects of propagation rate on displacement variations along faults. *Journal of Geophysical Research* 101, 311–320.
- Pickering, G., Bull, J.M., Sanderson, D.J., Harrison, P.V., 1994. Fractal fault displacements: a case study from the Moray Firth, Scotland. In: Kruhl, J.H. (Ed.), *Fractals and Dynamic Systems in Geosciences*. Springer, Berlin, pp. 105–118.
- Pollard, D.D., Segall, P., 1987. Theoretical displacements and stresses near fractures in rock; with applications to faults, joints, veins, dikes, and solution surfaces. In: Atkinson, B.K. (Ed.), *Fracture Mechanics of Rock*. Academic Press, London, pp. 277–349.
- Poulimenos, G., 2000. Scaling properties of normal fault populations in the western Corinth Graben, Greece: implications for fault growth in large strain settings. *Journal of Structural Geology* 27, 307–322.
- Read, S.A.L., 1984. The Ostler fault zone. In: Wood, P.R. (Ed.), *Guidebook to the South Island Scientific Excursions International Symposium on Recent Crustal Movements of the Pacific Region*. Wellington, NZ. February, 1984 Royal Society of New Zealand Miscellaneous Series 9. The Royal Society of New Zealand, Wellington, pp. 121–134.
- Schlichte, R.W., Young, S.S., Ackermann, R.V., Gupta, A., 1996. Geometry and scaling relations of a population of very small rift-related normal faults. *Geology* 24, 683–686.
- Scholz, C.H., 1982. Scaling laws for large earthquakes: consequences for physical models. *Bulletin of the Seismological Society of America* 72, 1–14.
- Scholz, C.H., 1990. *The Mechanics of Earthquakes and Faulting*. Cambridge University Press, Cambridge, UK.
- Scholz, C.H., Cowie, P.A., 1990. Fault growth and linkage models and distributions of fault length. *Nature* 346, 837–839.
- Scholz, C.H., Dawers, N.H., Yu, J.Z., Anders, M.H., 1993. Fault growth and fault scaling laws; preliminary results. In: Schubert, G. (Ed.), *Special Section on Physical Processes in Geodynamics [Modified]* 98. American Geophysical Union, Washington, pp. 21951–21961.
- Sempere, J.C., Macdonald, K.C., 1986. Overlapping spreading centers: implications from crack growth simulation by the displacement discontinuity method. *Tectonics* 5 (1), 151–163.
- Soliva, R., Benedicto, A., 2004. A linkage criterion for segmented normal faults. *Journal of Structural Geology* 26, 2251–2267.
- Suppe, J., Medwedeff, D.A., 1990. Geometry and kinematics of fault-propagation folding. *Eclogae Geologicae Helveticae* 83, 409–454.
- Tippett, J.M., Hovius, N., 2000. Geodynamic processes in the Southern Alps, New Zealand. In: Summerfield, M.A. (Ed.), *Geomorphology and Global Tectonics*. Wiley, Chichester, pp. 109–134.
- Turcotte, D.L., 1992. *Fractals and Chaos in Geology and Geophysics*. Cambridge University Press, Cambridge.
- Van Dissen, R.J., Hull, A.G., Read, S.A.L., 1993. Timing of Some Large Holocene Earthquakes on the Ostler Fault, New Zealand. *CRCM, Kobe, Japan*, pp. 381–386.
- Walcott, R.L., 1998. Modes of oblique compression; late Cenozoic tectonics of the South Island of New Zealand. *Reviews of Geophysics* 36, 1–26.
- Walsh, J.J., Watterson, J., 1988. Analysis of the relationship between displacements and dimensions of faults. *Journal of Structural Geology* 10, 239–247.
- Walsh, J.J., Nicol, A., Childs, C., 2002. An alternative model for the growth of faults. *Journal of Structural Geology* 24, 1669–1675.
- Walsh, J.J., Childs, C., Imber, J., Manzocchi, T., Watterson, J., Nell, P.A.R., 2003. Strain localisation and population changes during fault system growth within the Inner Moray Firth, Northern North Sea. *Journal of Structural Geology* 25, 307–315.
- Watterson, J., Walsh, J.J., Gillespie, A., Easton, S., 1996. Scaling systematics of fault sizes on a large-scale range fault map. *Journal of Structural Geology* 18, 199–214.
- Wells, D.L., Coppersmith, K.J., 1994. New empirical relationships among magnitude, rupture length, rupture width, rupture area, and surface displacement. *Bulletin of the Seismological Society of America* 84, 974–1002.
- Wickham, J., 1995. Fault displacement-gradient folds and the structure at Lost Hills, California. *Journal of Structural Geology* 17, 1293–1302.
- Willemsse, E.J.M., Pollard, D.D., Aydin, A., 1996. 3D analyses of slip distributions on normal fault arrays with consequences for fault scaling. *Journal of Structural Geology* 18, 295–309.